

All-optical magnetization control in CrI₃ monolayers: a microscopic theory

A. Kudlis,¹ M. Kazemi,² Y. Zhumagulov,³ H. Schrautzer,² P. F. Bessarab,^{2,4} I. V. Iorsh,¹ and I. A. Shelykh^{2,1}

¹*Abrikosov Center for Theoretical Physics, MIPT, Dolgoprudnyi, Moscow Region 141701, Russia**

²*Science Institute, University of Iceland, Dunhagi-3, IS-107 Reykjavik, Iceland[†]*

³*University of Regensburg, Regensburg 93040, Germany[‡]*

⁴*Department of Physics and Electrical Engineering, Linnaeus University, SE-39231 Kalmar, Sweden[§]*

(Dated: April 4, 2023)

Bright excitons in ferromagnetic monolayers CrI₃ efficiently interact with lattice magnetization, which makes possible all-optical resonant magnetization control in this material. Using the combination of ab-initio simulations within Bethe-Salpeter approach, semiconductor Bloch equations and Landau-Lifshitz equations, we construct a microscopic theory of this effect. Solving numerically the resulting system of the coupled equations describing the dynamics of atomic spins and spins of the excitons, we demonstrate the possibility of a tunable control of macroscopic magnetization of a sample.

I. INTRODUCTION

The search for effective ways to control the properties of layered structures is one of the current trends in both fundamental and applied research. In particular, the greatest demand exists in developing of the optimal methods of control of magnetic characteristics of materials. This is not surprising, given the ever-growing requirements for data-recording capacities of magnetic memory elements. The most important of them are compactness, energy efficiency, and recording speed. Regarding this latter, all-optical ways look very promising as compare to traditional approaches based on the application of external magnetic fields, as device operating frequencies can be in principle enhanced by several orders of magnitude.

To date, there already exists a number of theoretical [1, 2] and experimental works confirming the possibility of all-optical magnetic switching (AOMS) in a variety of magnetic compounds, including CdFeCo [3–7] and TbFeCo [8] ferromagnetic alloys, as well as in Pt/Co or Co/Gd multilayers [9, 10].

Among all candidates where such a reorientation is possible, materials combining ferromagnetic ordering with the presence of robust bright excitons, are of particular interest [11]. The examples of such materials are chromium trichalides, such as CrCl₃, CrBr₃ or CrI₃ [12]. In the current work we take CrI₃ as an example, but the reported results should remain qualitatively the same for other members of the family as well. In the material we consider, Cr³⁺ ions, are arranged in a honeycomb lattice organization and non-magnetic I⁻ ions. [13]. Being an 2D Ising ferromagnet, this material demonstrates robust optical excitonic response, with record high values of excitonic binding energies and oscillator strengths [14], exceeding even the values reported for transition metal dichalcogenides [15–18].

The combination of such unique properties allowed some of us to propose, that chromium trichalides are suitable candidates for polarization sensitive resonant op-

tical magnetization switching [19], which was later on confirmed experimentally [11]. The process of magnetic reorientation is connected with the transfer of angular momentum from excitons (electron-hole couples) to the lattice, and corresponding phenomenological theory was developed in Ref. 19. However, the full microscopic microscopic theory of the effect is still absent.

In this paper, we make an attempt to construct such microscopic theory. We apply the well-designed atomistic spin dynamics (ASD) formalism was taken as basis of our work and couple the corresponding equations for exciton dynamics, by adding the terms describing the interaction between the spins of the excitons and the magnetic lattice. Numerical solution of the resulting set of equations allows us to analyze in detail the dynamics of the magnetization switching in real space and time.

The paper is organized as follows. In Sec. II we present the calculation of the excitonic parameters in CrI₃, and then present the model Hamiltonian for coupled systems of excitons and lattice spins in Sec. III. Sec. IV presents the dynamic equations, and Sec. V contains the main results of the work, including the dependence of the properties, characterizing the process of the switching, on the parameters of the incident light beam. Sec. VI summarizes the results of the work.

II. DFT/BSE CALCULATIONS OF EXCITON PARAMETERS FOR CrI₃

We investigate the electronic structure of ferromagnetic CrI₃ monolayers via first-principles calculations employing density functional theory (DFT). The computations were executed using the GPAW package [20, 21], employing a plane wave basis with an energy cutoff of 600 eV and the LDA exchange-correlation functional, incorporating spin-orbit effects [22]. To mitigate interaction between periodic images, 16 Å vacuum was incorporated in the supercell.

Lattice constant determination for the CrI₃ ferromagnetic monolayer was achieved through crystal lattice re-

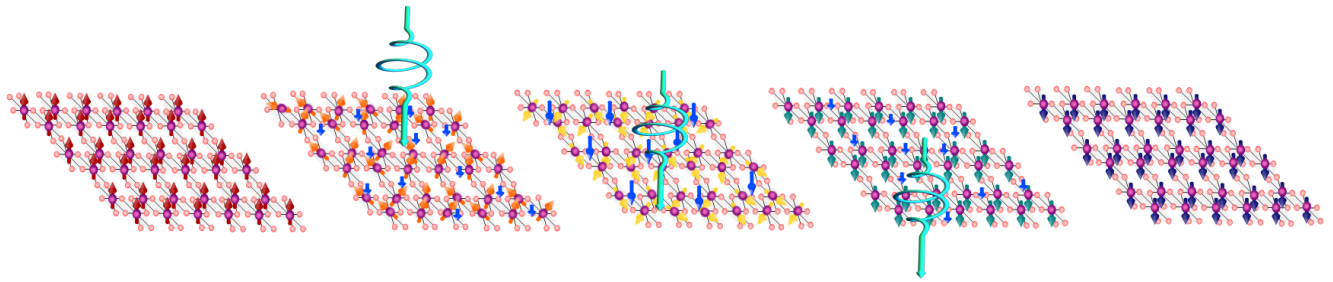


FIG. 1. Schematic representation of the optical magnetization switching. CrI₃ monolayer is irradiated by circularly polarized light. Optical pumping leads to the formation of excitons carrying magnetic moment defined by the pump helicity which interact with the lattice magnetization of the monolayer

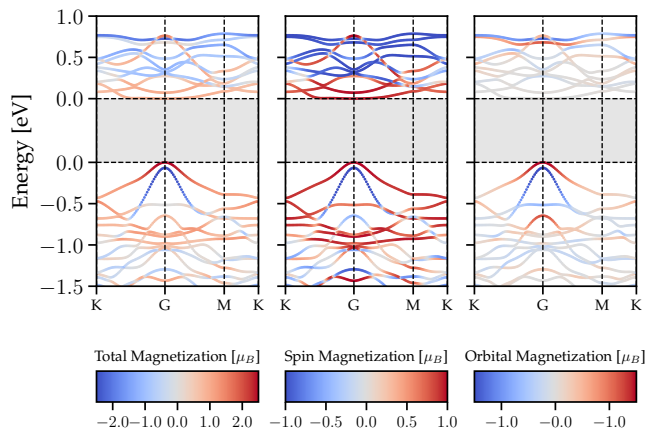


FIG. 2. DFT band structure of excitons in CrI₃ monolayer with lattice constant 6.69 Å. The color code shows orbital, spin and total magnetization in left, middle and right panel, respectively. The bandgap energy $E=2.59$ eV which is indicated by gray shading. According to the first Brillouin zone grid, we have selected 16 valence bands and 14 conduction bands for the exciton basis.

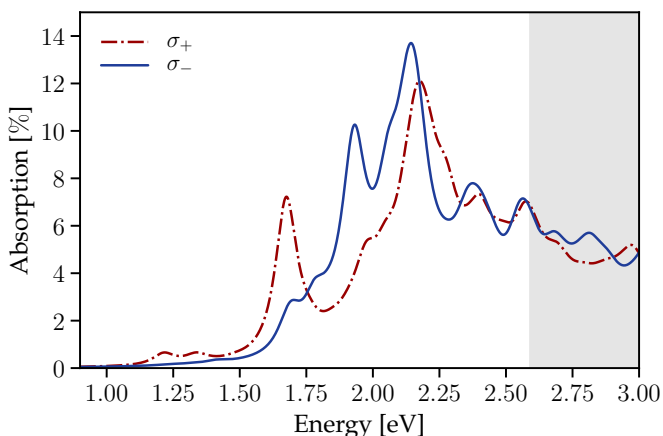


FIG. 3. Absorption spectrum of CrI₃ sample for two circular polarizations. The solid line corresponds to σ_- and dashed line to σ_+ polarization, respectively.

laxation procedures, resulting in a value of 6.69 Å. The

force convergence criteria were set at 1 meV/Å per atom. To address the DFT bandgap issue, a scissor operator was employed to adjust the bandgap value to the experimental value of 2.59 eV [14].

The exciton spectrum was acquired utilizing the GPAW implementation of the Bethe-Salpeter equation [23–26]. Screened Coulomb potential expressions were derived with a dielectric cutoff of 50 eV, 200 electronic bands, and a 2D truncated Coulomb potential [25]. The exciton basis was configured with 16 valence bands and 14 conduction bands on a 6x6 grid of the first Brillouin zone.

In Fig. 2 we demonstrate the band structure of CrI₃ monolayer with color bar for orbital, spin and total magnetization which shown below the main figures. The bandgap of 2.59 eV is schematically shown by gray bars. An analysis of the polarization resolved absorption spectrum of a CrI₃ monolayer is shown in Fig. 3. As one can see, there is a remarkable difference in absorption of σ_+ and σ_- components. The prominent absorption peaks in both the σ_+ and σ_- absorption profiles are related to the excitonic transitions. Naturally, if magnetization of the sample is inverted, the absorption curves corresponding to opposite polarizations interchange. This forms the basis of the magnetization switching mechanism: for a given pump frequency and polarization, the magnetic sublattice tends to orient its magnetization in a way to maximize absorption [19].

III. THE MODEL HAMILTONIAN

The Hamiltonian of the system reads:

$$H = H_m + H_{\text{exc}} + H_s, \quad (1)$$

where the first term describes the magnetic subsystem, the second term-excitonic subsystem, and the last term-the interaction between them. Let us consider these three terms consequently.

We model the magnetic structure of the CrI₃ monolayer in frameworks of the classical model of spins localized on sites of the honeycomb lattice of the Cr atoms. The corresponding classical extended Heisenberg Hamiltonian:

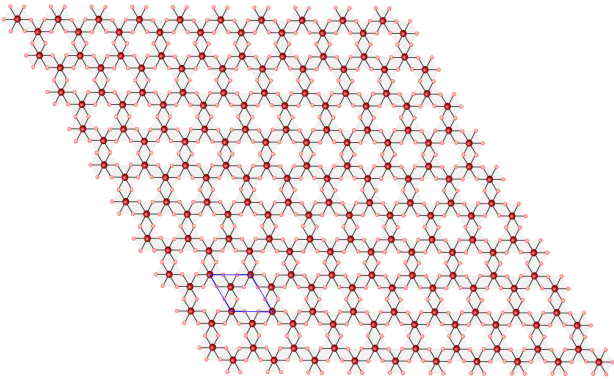


FIG. 4. CrI₃ structure. In this illustration, the atoms of chrome and iodine are represented by red and pink spheres, respectively. As shown in the figure, the unit cell of CrI₃ consists of two Cr atoms and six I atoms, with the Cr atoms forming a honeycomb structure.

$$H_m = - \sum_{\langle i,j \rangle} J \mathbf{m}_i \cdot \mathbf{m}_j - D \sum_{\langle i,j \rangle} \mathbf{d}_{ij} \cdot [\mathbf{m}_i \times \mathbf{m}_j] - K \sum_i (\mathbf{m}_i \cdot \mathbf{e}_z)^2 - \mu \mu_B \sum_i \mathbf{B} \cdot \mathbf{m}_i, \quad (2)$$

where $\mathbf{m}_i = \mathbf{S}_i/|\mathbf{S}_i|$ is the dimensionless magnetization direction at lattice site i . The magnetic moments \mathbf{S}_i are measured in units of Bohr magneton. In the order of appearance the interaction terms in Eq. 2 describe the Heisenberg exchange, the Dzyaloshinskii–Moriya interaction (DMI), the uniaxial magnetocrystalline anisotropy and the Zeeman interaction. The single spin interactions are summed over all lattice sites i . Assuming isotropic interactions the two-spin interactions are grouped into shells and we use nearest neighbor exchange of $J_1 = 2.53$ meV and nearest neighbor DMI of $|\vec{D}_1| = 1.2$ meV per bond. These parameters were taken from the atomistic simulations [27] for a honeycomb lattice of CrI₃, where skyrmions were reported for an uniaxial anisotropy of $K = 0.153$ meV per atom and a magnetic moment of $\mu = 3.0 \mu_B$. As one elementary cell of CrI₃ contains two magnetic atoms (see Fig. 4) the number of the magnetic atoms N_a is twice bigger than the number of elementary cells N_c , $N_a = 2N_c$. In all further calculations we use $N_c = 900$ (i. e. 30×30 grid).

To formulate the excitonic Hamiltonian, let us introduce the creation and annihilation operators of excitons in the state n with momentum \mathbf{q} , $\hat{X}_{n\mathbf{q}}^\dagger$ and $\hat{X}_{n\mathbf{q}}$ (note, that index n here denotes not a lattice site, but type of an exciton, different types of excitons correspond to different peaks in the absorption spectrum). We can then

write

$$\hat{H}_{\text{exc}} = \sum_{\mathbf{q}n} E_{n\mathbf{q}} \hat{X}_{n\mathbf{q}}^\dagger \hat{X}_{n\mathbf{q}} + \mathbf{E}_\pm \sum_n \mathbf{D}_{n\mathbf{q}=0} \hat{X}_{0\mathbf{q}=0}^\dagger \hat{X}_{n\mathbf{k}=0} + h.c., \quad (3)$$

where $E_{n\mathbf{q}}$ is the energy of an exciton, $\mathbf{D}_{n\mathbf{q}=0}$ is the dipole moment of the optical transition obtained from the DFT calculations (see Appendix C), here we limited ourselves to direct-gap transitions, $\mathbf{E}_\pm(t) = \text{Re}[(E_0, \mp iE_0, 0) \exp(-i\omega t)] h(t)$ is the right- or left-circularly polarized electric field characterized by pulse envelope $h(t)$.

The Hamiltonian of the interaction of the excitons and magnetic subsystems reads

$$\hat{H}_s = -g\mu \sum_{\mathbf{q}\mathbf{q}'nn'} (\mathbf{m}_{\mathbf{q}-\mathbf{q}'} - \mathbf{m}_{\mathbf{q}-\mathbf{q}'}^g) \mathbf{M}_{nn'}^{\mathbf{q}\mathbf{q}'} \hat{X}_{n\mathbf{q}}^\dagger \hat{X}_{n'\mathbf{q}'}, \quad (4)$$

where $\mathbf{m}(\mathbf{q} - \mathbf{q}')$ is Fourier transform of on-site-spin-vectors, $\mathbf{M}_{nn'}^{\mathbf{q}\mathbf{q}'}$ is dipole matrix element of interaction with local magnetic moment, g is the on-site spin-exciton coupling constant (see Appendix C for the details). The value of the coupling constant g requires a separate consideration and can not be determined in standard DFT approach. In this work it is taken as a phenomenological parameter with the value $g = 2.3$ meV, which is slightly less than the exchange interaction term in the lattice magnetic Hamiltonian.

IV. DYNAMIC EQUATIONS

Basing on the model Hamiltonian, we can derive the dynamic equations for physical observables describing the state of the system.

The dynamics of lattice magnetization is described by integrating the Landau-Lifshitz-Gilbert equation (LLGE) for normalized magnetization vectors at 0K. For this we use the semi-implicit solver by Mentink *et al.* [28]. Using a nonzero damping parameter in LLGE forces the system to converge into a local energy minimum. The corresponding equations are:

$$\frac{d\mathbf{m}_i}{dt} = -\gamma \mathbf{m}_i \times \mathbf{B}_i^{\text{eff}} + \eta \left(\mathbf{m}_i \times \frac{d\mathbf{m}_i}{dt} \right), \quad (5)$$

where η is the dimensionless damping parameter and $\mathbf{B}_i^{\text{eff}}$ is the effective magnetic field defined as:

$$\mathbf{B}_i^{\text{eff}} = -\frac{1}{\mu} \frac{\partial H}{\partial \mathbf{m}_i}, \quad (6)$$

where μ is the magnitude of the localized magnetic moments and H is the Hamiltonian of the system. We should take into account that, in fact, we model the dynamics of one exciton, multiplying its contribution to the

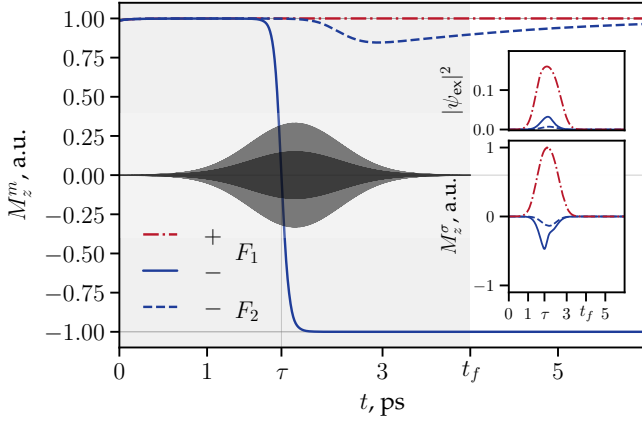


FIG. 5. Dependence of lattice magnetization vector component M_z^m on time for different light polarizations. Shaded area demonstrates the duration of laser pulse. The inset in the upper right corner shows the behavior of the square of the absolute value of all exciton state vector components. Lower right inset shows the time dependence of the exciton magnetization. Dark grey shaded area depicts the envelope function of the optical pump pulse. The transition time – point when average magnetization z -projection changes sign – is indicated by τ and here $\tau = 1.85$ ps. $F_1 = 166$ mJ/cm², while in the case of $F_2 = 33.2$ mJ/cm² there is no switching of magnetization. Damping constant η is 0.2. The dimensionless constants A and B in Eq. (11) are chosen as: $A = 1.94$, $B = 32.2$.

magnetization by the value of the exciton density at the end (because in this work we do not take into account the exciton-exciton interaction). Throughout the work we will use the following value, which is in some sense the upper bound (half of the number of cells): $n_{\text{exc}} = 450$. Thus, in case of lattice Hamiltonian the corresponding term (interaction contribution to H_m) can be obtained as:

$$H_s = n_{\text{exc}} \langle \Psi_{\text{exc}} | \hat{H}_s | \Psi_{\text{exc}} \rangle = -g\mu \sum_i \sigma_i (\mathbf{m}_i - \mathbf{m}_i^{\text{g}}), \quad (7)$$

where we characterized excitons by Pauli operators σ_i associated with individual elementary cells, which can be done, since an exciton in CrI₃ is of the Frenkel type. Thus, the final lattice Hamiltonian is $H = H_m + H_s$. In (7), we take the Fourier transform (see details A) and also used the excitonic wave function

$$\Psi_{\text{exc}} = \sum_{n\mathbf{q}} C_n^{\mathbf{q}} \hat{X}_{n\mathbf{q}}^\dagger |0\rangle. \quad (8)$$

Here, we also introduced the exciton spin σ_i for all sites of the analyzed lattice. It was defined by means of the following relation:

$$\mathbf{M}(\mathbf{r}) = n_{\text{exc}} \sum_{\mathbf{q}\mathbf{q}'} e^{2\pi i(\mathbf{r}(\mathbf{q}' - \mathbf{q}))_{N_c}} \sum_{nn'} C_n^{\mathbf{q}*} \mathbf{M}_{nn'}^{\mathbf{q}\mathbf{q}'} C_{n'}^{\mathbf{q}'}, \quad (9)$$

Note, that this quantity should be evaluated at each moment of time.

The corresponding dynamical equation of motion for Ψ_{exc} coefficients is:

$$i\hbar \frac{\partial C_n^{\mathbf{q}}}{\partial t} = \sum_{n'\mathbf{q}'} H_{nn'}^{\mathbf{q}\mathbf{q}'}(t) C_{n'}^{\mathbf{q}'}(t). \quad (10)$$

V. RESULTS AND DISCUSSION

To study the dynamics of the magnetization, we analyzed the case of a sample with spatially homogeneous initial polarization illuminated by spatially homogeneous circular polarized laser pulse at normal incidence. For maximum closeness to the real setups [11, 29] we choose the pulse envelope $h(t)$ as:

$$h(t) = A\theta(t_f - |2t - t_f|) \exp \left[-B \left(\frac{t - t_f/2}{t_f} \right)^2 \right], \quad (11)$$

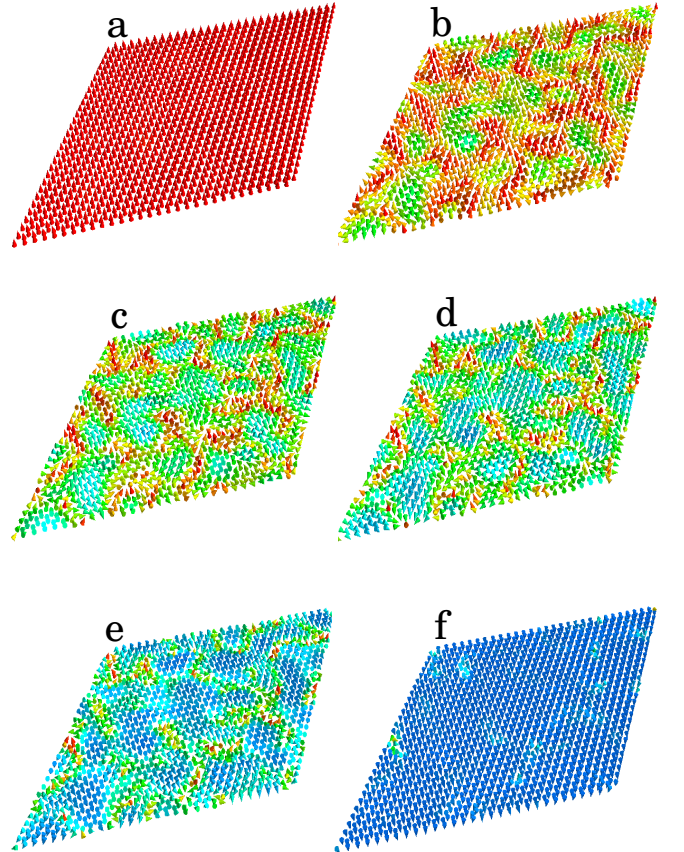


FIG. 6. (a)-(f) Snapshots(3D) of lattice magnetization profile at different moments of time during the switching process. Parameters for the calculation are the same as in Fig. 5. The case that corresponds to the F_1 value of fluence. The time moments are a) $\tau = 1.6$ ps, b) $\tau = 1.8$ ps, c) $\tau = 1.84$ ps, d) $\tau = 1.86$ ps, e) $\tau = 1.9$ ps, f) $\tau = 2.04$ ps.

where t_f is duration of the pulse, A and B are dimensionless constants affecting on the value of total pulse fluence defined as:

$$F = \frac{E_0^2 c \varepsilon_0}{2} \int_0^{t_f} h(t)^2 dt = C I_0 t_f, \quad (12)$$

where $C = A^2 \text{erf}(\sqrt{B/2}) \sqrt{\pi/(2B)}$.

We take the duration of the pulse $\tau_f = 4$ ps and its central frequency $\omega = 1.94$ eV, which is below the direct bandgap and corresponds to the vicinity of one of the σ^- peaks in absorption spectrum.

We monitor both the spatio-temporal pattern of the magnetization of the system, and cumulative magnetizations of the lattice and excitons, defined as:

$$M_z^m(t) = \frac{1}{N_a} \sum_{i=1}^{N_a} m_i^z(t), \quad M_z^\sigma(t) = \frac{1}{N_c} \sum_{i=1}^{N_c} \sigma_i^z(t), \quad (13)$$

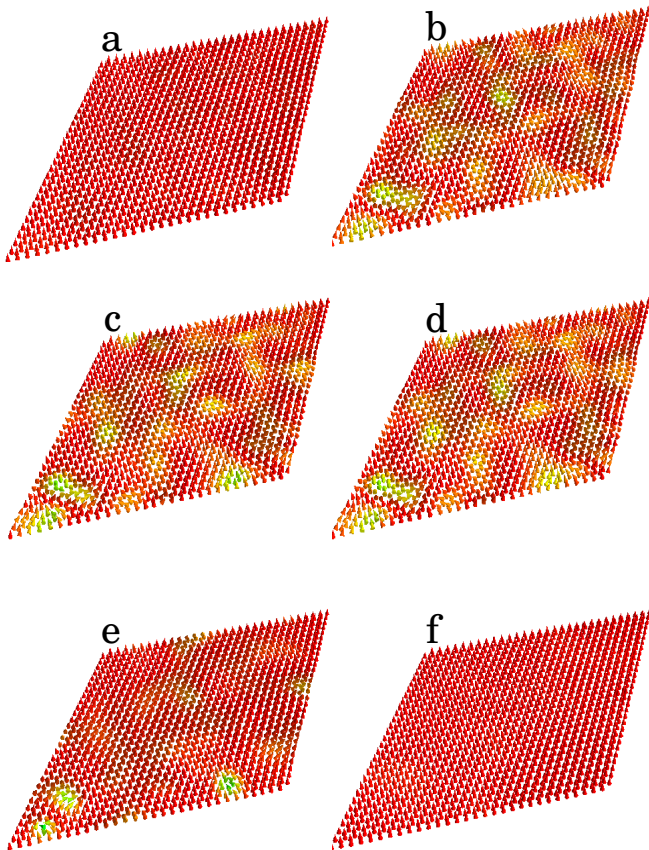


FIG. 7. (a)-(f) Snapshots(3D) of unswitched lattice magnetization in the following time. a) $\tau = 2.2$ ps, b) $\tau = 2.76$ ps, c) $\tau = 2.98$ ps, d) $\tau = 3.2$ ps, e) $\tau = 4.4$ ps, f) $\tau = 8.0$ ps. It is shown that, by using (left) circularly polarized pump and the fluence $F_2 = 33.2 \text{ mJ/cm}^2$, the magnetization cannot be switched. Corresponding to the dashed line in Fig. 5

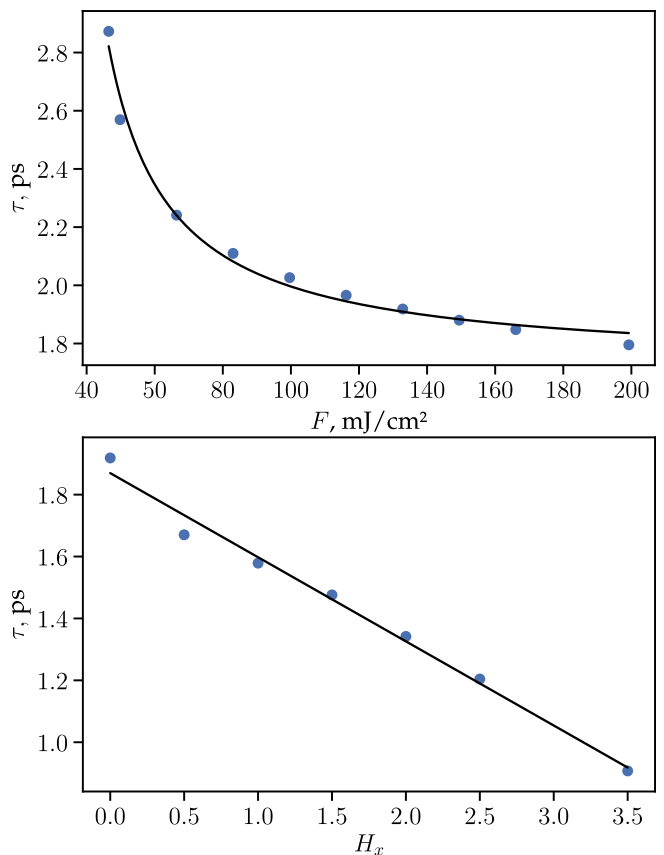


FIG. 8. Upper panel: The influence of pump fluence on transition time. The first optical magnetization switching is achieved at $F = 46.49 \text{ mJ/cm}^2$, under this value the magnetization remains unchanged after circularly polarized is applied. here all other parameters are the same as in Fig. 5. Lower panel: The dependence of the transition time τ on the lateral external magnetic field, at fixed value of the fluence ($F = 132.83 \text{ mJ/cm}^2$) of the circularly polarized pump. here damping is $\eta = 0.2$

The spatio-temporal dynamics of the magnetization switching is shown in Fig.6. Moreover in this figure because of the presence of DM interaction, we have magnetic vortices, as DM interaction is an important quantity to control the vortex in magnetic materials. Initially homogeneous state is polarized spin-up. The arrival of the pulse of σ^- polarization leads to the appearance of the domains, where magnetization is inverted, which are randomly distributed inside the sample. If the fluence exceeds some critical value (we take $F = 0.4 \text{ TW/cm}^2$ as an example, which corresponds to the experimental values reported in Refs. [11, 29]), the size of these domains grows with the course of time, and finally the system reaches the state with spatially homogeneous inverted magnetization (panels a-d). On the other hand, if the fluence is below the critical value, the system relaxes back to the homogeneous state without inversion (panels e-h).

The dynamics of the cumulative magnetization is shown in Fig. 5 for the same value of the fluence $F = 0.4$

TW/cm². One sees, that the transition between spin-up and spin-down polarized states induced by the pulse is pretty steep, and one can thus introduce the corresponding characteristic switching time τ , which depends on the fluence and decreased when the fluence increase (as it is shown in Fig.8. This dependence corresponds well to the one obtained by us previously in terms of the phenomenological model of resonant magnetization switching [19].

Naturally, the change of the circular polarization of the incident beam modifies drastically the magnetization dynamics: the switching will not occur for spin-up initial magnetization, but will take place for spin-down initial magnetization.

Generally, the transition time τ is the principal parameter that characterizes switching, which in Fig. 8. is shown. There is a decrease in τ that is associated with an increase in fluence which we achieved to the first optical magnetization switching in $F = 46.49$ mJ/cm² but under this value the magnetization remains unchanged. The transition time is affected by lateral magnetic field in Fig. 8.

VI. CONCLUSION

In conclusion, we developed a microscopic theory of all-optical resonant polarization-sensitive magnetization switching in monolayers of CrI₃. The effect is due to the combination of the peculiar optical selection rules for excitons in this material and efficient coupling of excitons to magnetic lattice. The spatio-temporal dynamics of the magnetization patterns under circular polarized pulses of was investigated, and the dependence of the parameters, characterizing the switching, on the parameters of the optical pulse was determined.

ACKNOWLEDGEMENTS

A.K, M.K and I.A.S. acknowledge support from Icelandic research fund (Rannis), project No. 163082-051. A.K. thanks I.A.S. for hospitality during his stay at Iceland. I.V.I and I.A.S acknowledge support from the joint RFBR-DFG project No. 21-52-12038. Y. V. Z. is grateful to the Deutsche Forschungsgemeinschaft (DFG, German Research Foundation) SPP 2244 (Project-ID 443416183) for the financial support.

Appendix A: Fourier transforms

Transforming meshes through Fourier and inverse Fourier transforms. It is slightly different from the standard notation, the thing is that gratings in real space(\mathbf{r}) and momentum space(\mathbf{q}) have different discreteness. The function $f(q_j)$ can be selected as an optional one. Thus,

the formulas we use are as follows:

$$f(\mathbf{r}_i) = \sum_j^{N_q^2} \exp [2\pi i(\mathbf{r}_i \mathbf{q}_j)_{N_c}] f(\mathbf{q}_j), \quad (\text{A1})$$

$$f(\mathbf{q}_j) = \frac{1}{N_c} \sum_i^{N_c} \exp [-2\pi i(\mathbf{r}_i \mathbf{q}_j)_{N_c}] f(\mathbf{r}_i), \quad (\text{A2})$$

where N_c is the number of lattice cells. We define the dot product $(\dots)_{N_c}$ as:

$$(\mathbf{r}\mathbf{q})_{N_c} = \frac{r_i^x q_j^x}{N_c^x} + \frac{r_i^y q_j^y}{N_c^y} + \frac{r_i^z q_j^z}{N_c^z}. \quad (\text{A3})$$

Throughout the work we use $N_c^x = N_c^y = 30$ and $N_c^z = 1$. Let us give a little comment on the calculation of $\mathbf{m}(\mathbf{q} - \mathbf{q}')$. Since the summation is carried out over the cells, and in each cell we have two magnetic atoms, we adhered to the following quite natural formula:

$$\mathbf{m}(\mathbf{q} - \mathbf{q}') = \frac{1}{N_c} \sum_i^{N_c} \exp [-2\pi i(\mathbf{r}_i (\mathbf{q} - \mathbf{q}'))_{N_c}] \quad (\text{A4}) \\ \times (\mathbf{m}_{2i} + \mathbf{m}_{2i-1}),$$

where we take the average value as the spin associated with the cell.

Appendix B: Matrix elements

In this study, matrix elements of the exciton Hamiltonian were computed through the resolution of the Bethe-Salpeter equation (BSE), which was parameterized via first-principles calculations grounded on density functional theory (DFT) outcomes. The subsequent exciton wave functions and associated energies were derived by diagonalizing the BSE Hamiltonian [23, 30, 31] as follows:

$$\sum_{c'v'k'} H_{cvkc'v'k'}^{BSE}(\mathbf{q}) A_{c'v'k'}^{n\mathbf{q}} = E^{n\mathbf{q}} A_{cv\mathbf{q}}^{n\mathbf{q}}, \quad (\text{B1})$$

Here, $H_{cvkc'v'k'}^{BSE}(\mathbf{q})$ represents the exciton Hamiltonian for excitons possessing momentum \mathbf{q} . Moreover, $A_{cv\mathbf{q}}^{n\mathbf{q}}$ and $E^{n\mathbf{q}}$ signify the n th exciton wave function and energy, respectively, with \mathbf{q} momentum. The indices c , v , and \mathbf{k} denote the conduction band, valence band, and single-particle momentum, respectively. The Hamiltonian H^{BSE} was calculated employing the Tamm-Dancoff approximation [30], which is particularly well-suited for wide-gap semiconductors. This approximation disregards the coupling between resonance and anti-resonance poles while preserving the Hermiticity of the Hamiltonian.

The calculation of dipole matrix elements is carried out utilizing the subsequent equation:

$$\mathbf{D}_{n\mathbf{q}=0} = \langle 0|\mathbf{r}|n\mathbf{q}=0\rangle = \sum_{cvk} A_{cvk}^{n\mathbf{q}=0} \langle v\mathbf{k}|\mathbf{r}|c\mathbf{k}\rangle, \quad (\text{B2})$$

where $\langle v\mathbf{k}|\mathbf{r}|\mathbf{c}\mathbf{k}\rangle$ signifies the single-particle dipole matrix element corresponding to the optical transition from the conduction band c to the valence band v with momentum \mathbf{k} .

One of the key ingredients of the exciton-skyrmion Hamiltonian interaction is the matrix elements of the exciton magnetic moment $\mathbf{M}_{nn'}^{\mathbf{q}\mathbf{q}'}$. These matrix elements were assembled from the matrix elements of the spin magnetic moment $\mathbf{S}_{nn'}^{\mathbf{q}\mathbf{q}'}$ and the orbital magnetic moment $\mathbf{L}_{nn'}^{\mathbf{q}\mathbf{q}'}$. The matrix elements of the spin magnetic moment were calculated from the single-particle spin moment:

$$\mathbf{S}_{nn'}^{\mathbf{q}\mathbf{q}'} = \sum_{c\mathbf{k}, c'\mathbf{k}'} (A_{c\mathbf{k}}^{n\mathbf{q}})^* A_{c'\mathbf{k}'}^{n'\mathbf{q}'} \times [\langle c\mathbf{k}+\mathbf{q}|\mathbf{S}|c'\mathbf{k}'+\mathbf{q}'\rangle - \langle v'\mathbf{k}'|\mathbf{S}|v\mathbf{k}\rangle], \quad (\text{B3})$$

where $\langle c\mathbf{k}|\mathbf{S}|c'\mathbf{k}'\rangle$ is the single-particle spin matrix elements between c band with \mathbf{k} momentum and c' band with \mathbf{k}' momentum. While the spin single-particle operators are simply defined using the Pauli matrices in the spin subspace, the calculation of the orbital moment requires a much more specific approach. In the present study, we employ a local projector augmented wave (PAW) technique to evaluate the orbital single-particle magnetic moment, as it offers a more straightforward approach compared to the previously reported perturbation theory-based methods [32–36]. All-electron orbitals inside PAW sphere can be expanded as [37, 38]

$$|\mathbf{c}\mathbf{k}\rangle = \sum_i \langle p_i^a | \tilde{\psi}_{\mathbf{c}\mathbf{k}} | \phi_i^a \rangle, \quad (\text{B4})$$

where ϕ_i^a is the i_{th} all-electron partial waves for a_{th} atom, is its projector p_i^a and $\tilde{\psi}_{\mathbf{c}\mathbf{k}}$ is smooth pseudowave function for c band with \mathbf{k} momentum. So, we calculated the one-particle matrix elements of the orbital momentum

as follows [22]:

$$\langle \mathbf{c}\mathbf{k}|\mathbf{L}|\mathbf{c}'\mathbf{k}'\rangle = \sum_{a i_1 i_2} \langle \tilde{\psi}_{\mathbf{c}\mathbf{k}} | p_{i_1}^a \rangle \langle \phi_{i_1}^a | \mathbf{L}^a | \phi_{i_2}^a \rangle \langle p_{i_2}^a | \tilde{\psi}_{\mathbf{c}'\mathbf{k}'} \rangle, \quad (\text{B5})$$

where \mathbf{L}^a is the orbital momentum operator for a atom. Since partial waves ϕ_i^a are usually defined on a spherical basis, the matrix elements $\langle \phi_{i_1}^a | \mathbf{L}^a | \phi_{i_2}^a \rangle$ can be calculated analytically. Having single-particle matrix elements of the orbital magnetic moment, we made up the exciton matrix elements as

$$\mathbf{L}_{nn'}^{\mathbf{q}\mathbf{q}'} = \sum_{c\mathbf{k}, c'\mathbf{k}'} (A_{c\mathbf{k}}^{n\mathbf{q}})^* A_{c'\mathbf{k}'}^{n'\mathbf{q}'} \times [\langle c\mathbf{k}+\mathbf{q}|\mathbf{L}|\mathbf{c}'\mathbf{k}'+\mathbf{q}'\rangle - \langle v'\mathbf{k}'|\mathbf{L}|v\mathbf{k}\rangle]. \quad (\text{B6})$$

The total exciton magnetic moment was obtained by adding the spin and orbital components:

$$\mathbf{M}_{nn'}^{\mathbf{q}\mathbf{q}'} = \mathbf{L}_{nn'}^{\mathbf{q}\mathbf{q}'} + \mathbf{S}_{nn'}^{\mathbf{q}\mathbf{q}'}. \quad (\text{B7})$$

Appendix C: Introduction of the damping

Obviously, the Hamiltonian (3) does not take into account both radiative and non-radiative damping processes which should affect. To account for it, we introduce the damping parameter γ , which, for simplicity, will be assumed to be the same for all excited excitonic states. By means of this parameter, any excited state ψ_i , $i > 0$ should change over time Δt as $|\psi_i|^2 \rightarrow |\psi_i|^2 \exp(-\Delta t \gamma)$. Thus, at each time step of evolution of the vector of state, $\Psi_{\text{exc}} = (\psi_0, \psi_1, \dots, \psi_n)$ where ψ_0 is the component responsible for vacuum, we do the following operations:

$$\psi_{i,\text{new}} = \psi_i \sqrt{1 - \Delta t \gamma}, \quad (\text{C1})$$

$$\Delta = 1 - \left(\sum_{i=1}^n |\psi_{i,\text{new}}|^2 + |\psi_0|^2 \right), \quad (\text{C2})$$

$$\psi_{0,\text{new}} = \psi_0 \frac{\sqrt{\Delta + |\psi_0|^2}}{|\psi_0|}, \quad (\text{C3})$$

and $\Psi_{\text{exc}} = \Psi_{\text{new}} = (\psi_{0,\text{new}}, \psi_{1,\text{new}}, \dots, \psi_{n,\text{new}})$, where $|\Psi| = |\Psi_{\text{new}}| = 1$. Throughout the article, we assume that the value of γ equals to 80 meV.

* kudlis.a@mipt.ru

† mak99@hi.is

‡ yaroslav.zhumagulov@gmail.com

§ bessarab@hi.is

- [1] J. Gorchon, R. B. Wilson, Y. Yang, A. Pattabi, J. Y. Chen, L. He, J. P. Wang, M. Li, and J. Bokor, “Role of electron and phonon temperatures in the helicity-independent all-optical switching of gdfco,” *Phys. Rev. B* **94**, 184406 (2016).
- [2] R. Moreno, T. A. Ostler, R. W. Chantrell, and O. Chubykalo-Fesenko, “Conditions for thermally induced all-optical switching in ferrimagnetic alloys: Mod-

eling of tbco,” *Phys. Rev. B* **96**, 014409 (2017).

- [3] D. O. Ignatyeva, C. S. Davies, D. A. Sylgacheva, A. Tsukamoto, H. Yoshikawa, P. O. Kapralov, A. Kirilyuk, V. I. Belotelov, and A. V. Kimel, “Plasmonic layer-selective all-optical switching of magnetization with nanometer resolution,” *Nature Comm.* **10**, 4786 (2019).
- [4] L. Aviles-Flix, A. Olivier, G. Li, C. S. Davies, L. Alvaro-Gomez, M. Rubio-Roy, S. Auffret, A. Kirilyuk, A. V. Kimel, Th. Rasing, L. D. Buda-Prejbeanu, R. C. Sousa, B. Dieny, and I. L. Prejbeanu, “Single-shot all-optical switching of magnetization in tb/co multilayer-based electrodes,” *Sci. Rep.* **10**, 5211 (2020).

- [5] C. D. Stanciu, F. Hansteen, A. V. Kimel, A. Kirilyuk, A. Tsukamoto, A. Itoh, and Th. Rasing, “All-optical magnetic recording with circularly polarized light,” *Phys. Rev. Lett.* **99**, 047601 (2020).
- [6] C. S. Davies, T. Janssen, J. H. Mentink, A. Tsukamoto, A. V. Kimel, A. F. G. van der Meer, A. Stupakiewicz, and A. Kirilyuk, “Pathways for single-shot all-optical switching of magnetization in ferrimagnets,” *Phys. Rev. Applied* **13**, 024064 (2020).
- [7] J. Igarashi, Q. Remy, S. Iihama, G. Malinowski, M. Hehn, J. Gorchon, J. Hohlfield, S. Fukami, H. Ohno, and S. Mangin, “Engineering single-shot all-optical switching of ferromagnetic materials,” *Nano Lett.* **20**, 8654 (2020).
- [8] X. Lu, X. Zou, D. Hinzke, T. Liu, Y. Wang, T. Cheng, J. Wu, T. A. Ostler, J. Cai, U. Nowak, R. W. Chantrell, Y. Zhai, and Y. Xu, “Roles of heating and helicity in ultrafast all-optical magnetization switching in tbfeo,” *Appl. Phys. Lett.* **113**, 032405 (2018).
- [9] M. S. El Hadri, P. Pirro, C.-H. Lambert, S. Petit-Watelot, Y. Quessab, M. Hehn, F. Montaigne, G. Malinowski, and S. Mangin, “Two types of all-optical magnetization switching mechanisms using femtosecond laser pulses,” *Phys. Rev. B* **94**, 064412 (2016).
- [10] Y. L. W. van Hees, P. van de Meughevel, B. Koopmans, and R. Lavrijsen, “Deterministic all-optical magnetization writing facilitated by non-local transfer of spin angular momentum,” *Nature Comm.* **11**, 3835 (2020).
- [11] Peiyao Zhang, Ting-Fung Chung, Quanwei Li, Siqi Wang, Qingjun Wang, Warren L. B. Huey, Sui Yang, Joshua E. Goldberger, Jie Yao, and Xiang Zhang, “All-optical switching of magnetization in atomically thin CrI₃,” *Nature Materials* **21**, 1373–1378 (2022).
- [12] Bevin Huang, Genevieve Clark, Dahlia R Klein, David MacNeill, Efrén Navarro-Moratalla, Kyle L Seyler, Nathan Wilson, Michael A McGuire, David H Cobden, Di Xiao, *et al.*, “Electrical control of 2d magnetism in bilayer CrI₃,” *Nature nanotechnology* **13**, 544–548 (2018).
- [13] Michael A McGuire, Hemant Dixit, Valentino R Cooper, and Brian C Sales, “Coupling of crystal structure and magnetism in the layered, ferromagnetic insulator CrI₃,” *Chemistry of Materials* **27**, 612–620 (2015).
- [14] M. Wu, Z. Li, T. Cao, and S. G. Louie, “Physical origin of giant excitonic and magneto-optical responses in two-dimensional ferromagnetic insulators,” *Nature Comm.* **10**, 2371 (2019).
- [15] A. Chernikov, T. C. Berkelbach, H. M. Hill, A. Rigosi, Y. Li, O. B. Aslan, D. R. Reichman, M. S. Hybertsen, and T. F. Heinz, “Exciton binding energy and nonhydrogenic rydberg series in monolayer WS₂,” *Phys. Rev. Lett.* **113**, 076802 (2014).
- [16] A. Splendiani, L. Sun, Y. Zhang, T. Li, J. Kim, C.-Y. Chim, G. Galli, and F. Wang, “Emerging photoluminescence in monolayer MoS₂,” *Nano Lett.* **10**, 1271 (2010).
- [17] P. Steinleitner, P. Merkl, P. Nagler, J. Mornhinweg, C. Schüller, T. Korn, A. Chernikov, and R. Huber, “Direct observation of ultrafast exciton formation in a monolayer of WSe₂,” *Nano Lett.* **17**, 1455 (2017).
- [18] G. Wang, A. Chernikov, M. M. Glazov, T. F. Heinz, X. Marie, T. Amand, and B. Urbaszek, “Colloquium: Excitons in atomically thin transition metal dichalcogenides,” *Rev. Mod. Phys.* **90**, 021001 (2018).
- [19] A. Kudlis, I. Iorsh, and I. A. Shelykh, “All-optical resonant magnetization switching in CrI₃ monolayers,” *Phys. Rev. B* **104**, L020412 (2021).
- [20] J. J. Mortensen, L. B. Hansen, and K. W. Jacobsen, “Real-space grid implementation of the projector augmented wave method,” *Physical Review B* **71** (2005), 10.1103/physrevb.71.035109.
- [21] J. Enkovaara, C. Rostgaard, J. J. Mortensen, J. Chen, M. Dulak, L. Ferrighi, J. Gavnholt, C. Glinsvad, V. Haikola, H. A. Hansen, H. H. Kristoffersen, M. Kuisma, A. H. Larsen, L. Lehtovaara, M. Ljungberg, O. Lopez-Acevedo, P. G. Moses, J. Ojanen, T. Olsen, V. Petzold, N. A. Romero, J. Stausholm-Møller, M. Strange, G. A. Tritsarolis, M. Vanin, M. Walter, B. Hammer, H. Häkkinen, G. K. H. Madsen, R. M. Nieminen, J. K. Nørskov, M. Puska, T. T. Rantala, J. Schiøtz, K. S. Thygesen, and K. W. Jacobsen, “Electronic structure calculations with GPAW: a real-space implementation of the projector augmented-wave method,” *Journal of Physics: Condensed Matter* **22**, 253202 (2010).
- [22] Thomas Olsen, “Designing in-plane heterostructures of quantum spin hall insulators from first principles: 1t′-MoS₂ with adsorbates,” *Phys. Rev. B* **94**, 235106 (2016).
- [23] Michael Rohlfing and Steven G. Louie, “Electron-hole excitations and optical spectra from first principles,” *Phys. Rev. B* **62**, 4927–4944 (2000).
- [24] Jun Yan, Jens. J. Mortensen, Karsten W. Jacobsen, and Kristian S. Thygesen, “Linear density response function in the projector augmented wave method: Applications to solids, surfaces, and interfaces,” *Phys. Rev. B* **83**, 245122 (2011).
- [25] Falco Hüser, Thomas Olsen, and Kristian S. Thygesen, “How dielectric screening in two-dimensional crystals affects the convergence of excited-state calculations: Monolayer MoS₂,” *Phys. Rev. B* **88**, 245309 (2013).
- [26] Thomas Olsen, “Unified treatment of magnons and excitons in monolayer CrI₃ from many-body perturbation theory,” *Phys. Rev. Lett.* **127**, 166402 (2021).
- [27] Sukanya Ghosh, Nataša Stojić, and Nadia Binggeli, “Comment on “magnetic skyrmions in atomic thin CrI₃ monolayer” [appl. phys. lett. 114, 232402 (2019)],” *Applied Physics Letters* **116**, 086101 (2020).
- [28] JH Mentink, MV Tretyakov, A Fasolino, MI Katsnelson, and Th Rasing, “Stable and fast semi-implicit integration of the stochastic Landau-Lifshitz equation,” *Journal of Physics: Condensed Matter* **22**, 176001 (2010).
- [29] Dachbrowski Maciej, Guo Shi, Strungaru Mara, S. Keatley Paul, Withers Freddie, Elton J. G. Santos, and Robert J. Hicken, “All-optical control of spin in a 2d van der Waals magnet,” *Nature Communications* **13** (2022), 10.1038/s41467-022-33343-4.
- [30] Giovanni Onida, Lucia Reining, and Angel Rubio, “Electronic excitations: density-functional versus many-body Green’s-function approaches,” *Rev. Mod. Phys.* **74**, 601–659 (2002).
- [31] Michael Rohlfing and Steven G. Louie, “Electron-hole excitations in semiconductors and insulators,” *Phys. Rev. Lett.* **81**, 2312–2315 (1998).
- [32] Thorsten Deilmann, Peter Krüger, and Michael Rohlfing, “Ab initio studies of exciton *g* factors: Monolayer transition metal dichalcogenides in magnetic fields,” *Phys. Rev. Lett.* **124**, 226402 (2020).
- [33] Tomasz Woźniak, Paulo E. Faria Junior, Gotthard Seifert, Andrey Chaves, and Jens Kunstmann, “Exciton *g* factors of van der Waals heterostructures from first-principles calculations,” *Phys. Rev. B* **101**, 235408 (2020).

- [34] M. G. Lopez, David Vanderbilt, T. Thonhauser, and Ivo Souza, “Wannier-based calculation of the orbital magnetization in crystals,” *Phys. Rev. B* **85**, 014435 (2012).
- [35] T. Thonhauser, Davide Ceresoli, David Vanderbilt, and R. Resta, “Orbital magnetization in periodic insulators,” *Phys. Rev. Lett.* **95**, 137205 (2005).
- [36] Davide Ceresoli, T. Thonhauser, David Vanderbilt, and R. Resta, “Orbital magnetization in crystalline solids: Multi-band insulators, chern insulators, and metals,” *Phys. Rev. B* **74**, 024408 (2006).
- [37] J. J. Mortensen, L. B. Hansen, and K. W. Jacobsen, “Real-space grid implementation of the projector augmented wave method,” *Phys. Rev. B* **71**, 035109 (2005).
- [38] P. E. Blöchl, “Projector augmented-wave method,” *Phys. Rev. B* **50**, 17953–17979 (1994).